

PAPER • OPEN ACCESS

# Observation of local density increase during pellet homogenization on EAST











To cite this article: J. Huang *et al* 2024 *Nucl. Fusion* **64** 016031

View the [article online](#) for updates and enhancements.

## You may also like

- [Comparative study of two different reflectors, zincalume steel and aluminum foil tape in the application of solar cookers](#)  
S Nurul Amalia Silviyanti and Santoso
- [The effectiveness of ICRT Video-based Reflection System on Pre-service Teachers' Micro Teaching Practice Focusing on Meaningful Learning with ICT](#)  
K F Ratumbuisang, Y T Wu and H D Surjono
- [Development of static solar panel equipped by an active reflector based on LDR sensors](#)  
W Indrasari, R Fahdiran, E Budi et al.

# Observation of local density increase during pellet homogenization on EAST

J. Huang<sup>1,2,3</sup> , T. Zhang<sup>2,\*</sup> , J. Zhang<sup>1,\*</sup>, Y.F. Liang<sup>3</sup> , Y.M. Wang<sup>6,7</sup>, L. Liao<sup>1,2,3</sup>, J.L. Hou<sup>2</sup> , X. Han<sup>2</sup>, K.X. Ye<sup>2</sup> , K.N. Geng<sup>2</sup> , H.M. Xiang<sup>3,4,5</sup> , F. Wen<sup>2</sup>, F.B. Zhong<sup>2</sup>, G.S. Li<sup>2</sup>, M.F. Wu<sup>2</sup>, Z. Zhou<sup>1,2</sup>, S.Q. Yang<sup>1,2</sup>, Z.Q. Zhou<sup>1,2</sup>, L. Yu<sup>1,2</sup>, H.Q. Liu<sup>2</sup> , A. Krämer-Flecken<sup>3</sup> , X. Gao<sup>2</sup> , G. Zhuang<sup>1</sup> and the EAST Team<sup>a</sup>

<sup>1</sup> University of Science and Technology of China, Hefei, Anhui 230026, China

<sup>2</sup> Institute of Plasma Physics, Chinese Academy of Sciences, Hefei, Anhui 230031, China

<sup>3</sup> Forschungszentrum Jülich GmbH, Institut für Energie- und Klimaforschung-Plasmaphysik, Partner of the Trilateral Euregio Cluster (TEC), 52425 Jülich, Germany

<sup>4</sup> Advanced Energy Research Center, Shenzhen University, Shenzhen 518060, China

<sup>5</sup> Key Laboratory of Optoelectronic Devices and Systems of Ministry of Education and Guangdong Province, College of Optoelectronic Engineering, Shenzhen University, Shenzhen 518060, China

<sup>6</sup> Hebei Key Laboratory of Compact Fusion, Langfang 065001, China

<sup>7</sup> ENN Science and Technology Development Co., Ltd, Langfang 065001, China

E-mail: [zhangt@ipp.ac.cn](mailto:zhangt@ipp.ac.cn) and [jiez111@ustc.edu.cn](mailto:jiez111@ustc.edu.cn)

Received 24 August 2023, revised 6 November 2023

Accepted for publication 22 November 2023

Published 5 December 2023



## Abstract

By combining the X-mode polarized lower and upper cut-off reflections obtained from the density profile reflectometer, we have successfully attained a comprehensive density profile spanning from the edge to the core region in pellet injection (PI) experiments on EAST. During the homogenization process after PI on EAST, an innovative method was introduced to quantify the local density increase. This approach employed the distinctive ‘dual-reflection’ phenomenon observed in the EAST microwave reflectometer, encompassing measurements of both the X-mode lower and upper cut-off frequencies. Furthermore, experimental investigations were carried out on EAST to comprehensively explore the parallel and poloidal expansion of the high-density pellet cloud. Notably, this study marks the first instance of measuring expansion velocities of pellet materials in both parallel and poloidal directions on EAST. A comparative analysis was performed initially between these experimental measurements and simulation results obtained from the HPI2 code, marking a pivotal stride towards enhancing its applicability in EAST.

**Keywords:** local density increase, pellet injection, homogenization, density profile reflectometer, EAST

(Some figures may appear in colour only in the online journal)

<sup>a</sup> See Wan *et al* 2017 (<https://doi.org/10.1088/1741-4326/aa7861>) for the EAST Team.

\* Authors to whom any correspondence should be addressed.



Original Content from this work may be used under the terms of the [Creative Commons Attribution 4.0 licence](https://creativecommons.org/licenses/by/4.0/). Any further distribution of this work must maintain attribution to the author(s) and the title of the work, journal citation and DOI.

## 1. Introduction

Cryogenic deuterium pellet injection (PI), due to its exceptionally high fueling efficiency, is considered to be the predominant method for plasma fueling in ITER. In future fusion devices, beyond its essential role in core plasma fueling, PI is anticipated to hold significant relevance in diverse domains, including triggering L–H transitions and controlling edge localized mode (ELM). Considerable endeavors have been directed towards comprehending the impacts of PI on plasma behavior, encompassing both experimental investigations and theoretical simulation analyses [1, 2].

The investigation of ablation and homogenization processes of pellet materials has emerged as a focal point in contemporary PI research. The pellet ablation process, observable through CCD cameras or arrays of  $H_\alpha$  emission detectors [3], finds comprehensive explanation through the neutral gas shielding model introduced in 1977 [4]. When considering the deposition and homogenization processes, the enhancement in temporal and spatial resolutions for local density measurement becomes of utmost importance in gaining insights into both parallel and poloidal expansion of ablated pellet materials (hereafter named plasmoid [5]). The comparative analysis of experimental measurements with simulation results detailing local density evolution offers a promising avenue for refining pellet simulation codes [6, 7].

Presently, significant attention has been directed towards both experimental and theoretical investigations of the ablation process subsequent to PI [1, 8–10]. The realm of theoretical simulations has also made substantial contributions to PI studies. The non-linear MHD code JOREK has been utilized in DIII-D [11] and JET [12]. As shown in figure 10 of [12], the local high-density region caused by pellet ablation expands simultaneously along parallel and perpendicular magnetic field lines, with the parallel expansion velocity approaching the local ion sound speed  $C_{s0}$ . However, a noticeable gap persists in the experimental exploration during the homogenization process of ablated particles. In the context of such research, an interferometer coupled with an x-ray camera for line-integrated density measurements were employed in TFTR, revealing the velocity of parallel expansion along the magnetic field of pellet ablatant [8, 13]. It was found that the entire homogenization period lasted less than 1 ms, with the parallel expansion velocity gradually decreasing from approximately  $1 \times 10^5 \text{ m s}^{-1}$  at its initiation to around  $3 \times 10^4 \text{ m s}^{-1}$  after roughly 200  $\mu\text{s}$ . In LHD [9], the ablation and assimilation processes of pellet particles were scrutinized using fast Thomson scattering [14], albeit within a limited temporal scope (sub-millisecond). In order to deepen our understanding of the physical mechanisms underlying the parallel and perpendicular expansion of ablated particles, there exists a pressing need for high-resolution local-density diagnostic measurements, exemplified by the reflectometer technique.

A multitude of PI experiments have been extensively conducted on the EAST tokamak, encompassing a diverse range

of scenarios such as plasma fueling, ELM pacing, L–H transition, and H–L back transition [15–17]. In the present study, our primary focus lies in investigating the edge-localized density increase induced by pellet deposition. This paper is structured as follows: section 2 presents the experimental setup. In section 3, the observation of local density increase after PI on EAST is presented. Section 4 offers insights into the parallel and poloidal expansion during pellet homogenization. Finally, we delve into discussions and provide a summary in sections 5 and 6, respectively.

## 2. Experimental setup

EAST, a superconducting tokamak, features a non-circular configuration with a major radius of  $R_0 = 1.85 \text{ m}$  and a minor radius of  $a = 0.45 \text{ m}$ . In this work, a series of pellets were continuously injected into L-mode plasma on EAST, adhering to specific discharge conditions: plasma current  $I_p = 0.4 \text{ MA}$ , toroidal magnetic field  $B_t = 2.42 \text{ T}$  in the anti-clockwise direction from bird-view, vertical elongation  $\kappa \sim 1.57$ , and edge safety factor  $q_{95} \sim 6.41$ . The plasma under an upper-single-null configuration is subject to heating from both lower hybrid current drive and neutral beam injection.

During the typical PI discharge #87924 on EAST, the temporal evolution of local density at a radial position of  $R = 2.28 \text{ m}$  and the line-integrated densities, measured by reflectometer and POINT respectively, is shown in figure 1. The injection of pellets is indicated by red arrows in this figure. For the measurement of both edge and core line-integrated densities, an 11-chord Polarimeter-INTERferometer (POINT) system positioned at the O-port of EAST with a temporal resolution of 4  $\mu\text{s}$  was employed [18]. For present analyzed experiment, only six out of the eleven channels of POINT diagnostics are available. Over the time span from 2.5 s to 4.1 s, pellets were injected into the plasma at a frequency of 10 Hz, consequently leading to a pronounced increase in both edge and core line-integrated densities.

The configuration of the PI system and the principal density diagnostics adopted for this study are depicted in figure 2. The edge magnetic field lines in the range of  $\rho = 0.9 \rightarrow 0.8$  are represented by gray dotted lines. The positions corresponding to the 11-channel POINT diagnostic system are indicated by dotted lines. Density profiles characterized by both high spatial ( $\sim 5 \text{ mm}$ ) and temporal (50  $\mu\text{s}$ ) resolution can be acquired using a fast frequency-sweeping microwave reflectometer system situated at the mid-plane of the low-field side (LFS) within the J-port on the EAST [19]. This reflectometer is composed of sub-systems operating across Q [19], V [20], and W [21] bands, effectively covering probing frequencies ranging from 33 GHz to 110 GHz. Since 2012, a PI system for plasma fueling has been developed on EAST [22]. The pellet injector is positioned at 0.42 m above the mid-plane in J-port ( $z \sim 0.42 \text{ m}$ ), same toroidal port as reflectometer on EAST. Each pellet takes on a cylindrical shape, possessing a diameter and length of 2 mm, and encapsulating an estimated  $3.8 \times 10^{20}$

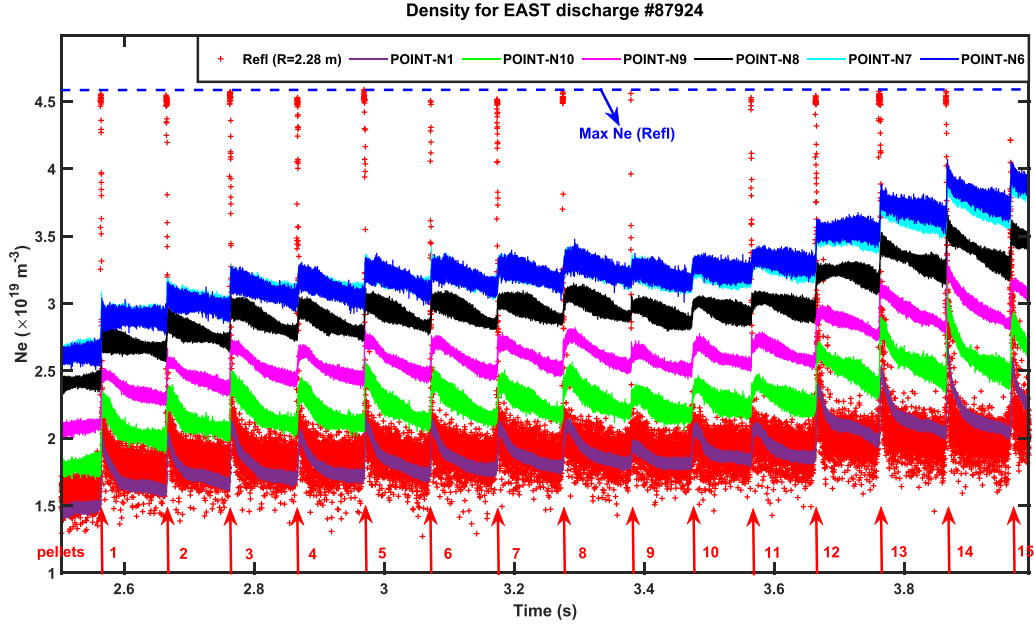


**Figure 1.** Temporal evolution of local density at a radial position of  $R=2.28$  m and the line-integrated densities. Injection of pellets is indicated by red arrows. The line-integrated densities measured by POINT are shown by the solid lines. The local density at  $R=2.28$  m measured by reflectometer (Refl) is indicated by red dots. Additionally, the upper limit of density measurement capability by the reflectometer at the same radial position is denoted by a blue dashed line.

atoms. The injection process is subject to a maximum velocity constraint of  $100 \text{ m s}^{-1}$  and a frequency ceiling of  $10 \text{ Hz}$  [23].

### 3. Observation of local density increase after PI

On EAST, the LFS PI system is located at the J-port ( $z=0.42$  m), the measurement window of the profile reflectometer is situated at the mid-plane of the J-port ( $z=0$  m), and the 8th channel of the POINT diagnostic is positioned at the O-port ( $z=-0.17$  m).

#### 3.1. Measurement of the X-mode polarization reflectometer

**3.1.1. Dual-reflection of W-band upper cut-off probing microwave.** The fast frequency-sweeping microwave reflectometer stands as an established diagnostic system for plasma density measurement [24]. This approach entails the emission of electromagnetic waves into a non-uniform plasma environment. At the cutoff layer where probing microwaves are reflected, the refractive index drops to zero. According to the frequency of the probing wave, the plasma density and the background magnetic field and the time delay of the probing wave propagating in the plasma, it becomes feasible to infer the cut-off position and density of plasma [25].

Figure 3 shows the measurement of group delay in fast frequency-sweeping density profile reflectometer after the 2nd PI at 2665 ms on EAST. The microwave source comprises an arbitrary waveform generator and a voltage controlled oscillator. The output frequency is multiplied to Q-, V- and W-band probing frequencies through different frequency multipliers [21]. Operating with a sweeping period of  $40 \mu\text{s}$  and

a subsequent pause period of  $10 \mu\text{s}$ , the reflectometer system facilitates a robust analysis of the temporal evolution of density profiles during the homogenization process at  $50 \mu\text{s}$  intervals. Figures 3(b)–(d) present the group delay spectra observed by X-mode polarization reflectometer at Q-, V- and W-band, respectively. In the high-density experiments under strong magnetic fields conditions on EAST, Q-band sub-system is utilized for receiving the lower cut-off reflections [26], while V- and W-band sub-systems are employed for the upper cut-off reflections. The boundary between these two reflections is defined by a zero-density layer within the V-band, which is characterized by a hopping in group delay when the probing frequency equals the electron cyclotron frequency ( $f_{\text{probing}} = f_{\text{ece}}$ ). Specific application regarding utilization of the lower cut-off frequency during density profile inversion on EAST has been described detailedly in [26]. As shown in figure 3(b), the Q-band sub-system demonstrates a lower cut-off reflection and a gradual increase in signal intensity with the increasing plasma density after PI. In figure 3(d), the upper cut-off reflections progressively shift from high-group-delay ( $\tau_p = 15 \sim 23$  ns) before PI to low-group-delay ( $\tau_p = 10 \sim 15$  ns) after PI, with an intermediate transitional state observed during  $2665.2 \text{ ms} \rightarrow 2665.3 \text{ ms}$ .

As shown in figure 2, deuterium pellets are horizontally injected into plasma from LFS at a height of  $0.42$  m above the middle plane of J-port. The high-density plasmoid swiftly undergo an expansion along the magnetic field lines. This expansion leads them towards the diagnostic window of the J-port density profile reflectometer and subsequently progresses to reach the measurement position corresponding to the 8th chord of the O-port POINT diagnostic system. As ascertained by the reflectometer at the middle plane of

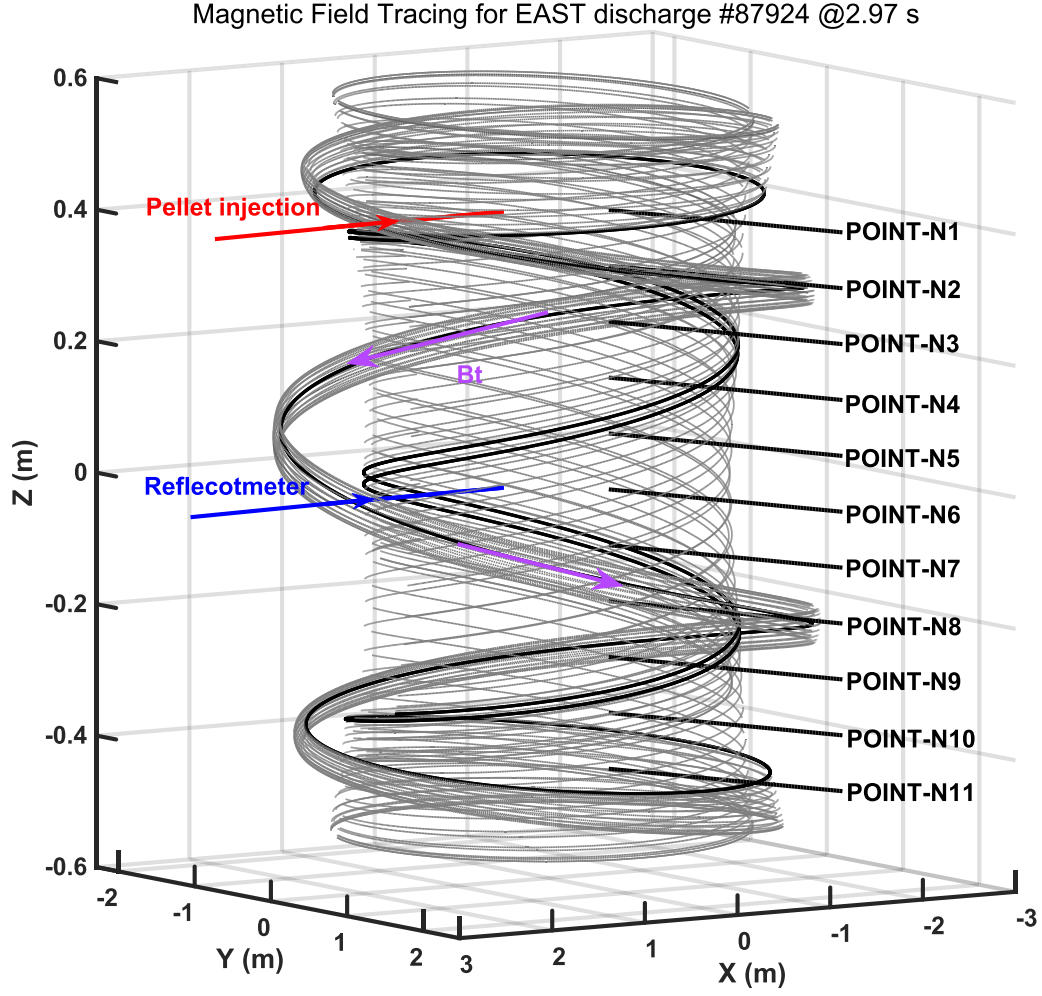


**Figure 2.** The layout of key diagnostics and LFS PI system on EAST. The tracing of edge magnetic field line in the range of  $\rho = 0.8 \sim 0.9$  (gray dotted lines). The location of PI is highlighted with a red arrow, while the position of reflectometer diagnostic window is indicated by a blue arrow. The positions corresponding to the 11-channel POINT diagnostic system are indicated by black horizontal lines.

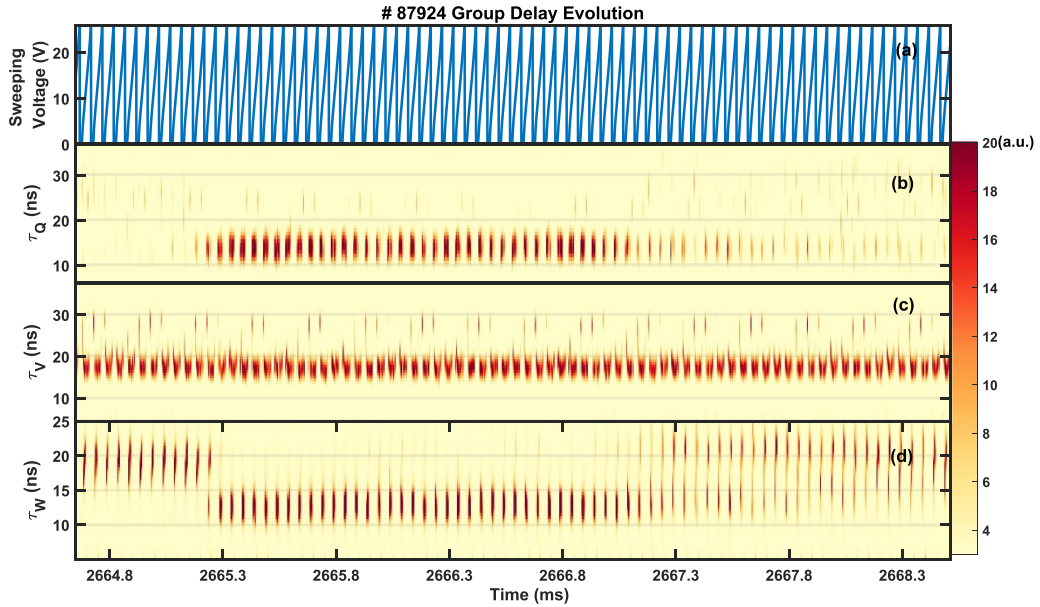


**Figure 3.** Evolution of group delay in density profile reflectometer after 2nd PI at 2665 ms. (a) Input of VCO in reflectometer and group delay measured by (b) Q-band (33 → 50 GHz); (c) V-band (50 → 75 GHz); (d) W-band (75 → 110 GHz) reflectometer. The color bar on the right indicates the power of the reflected microwave.



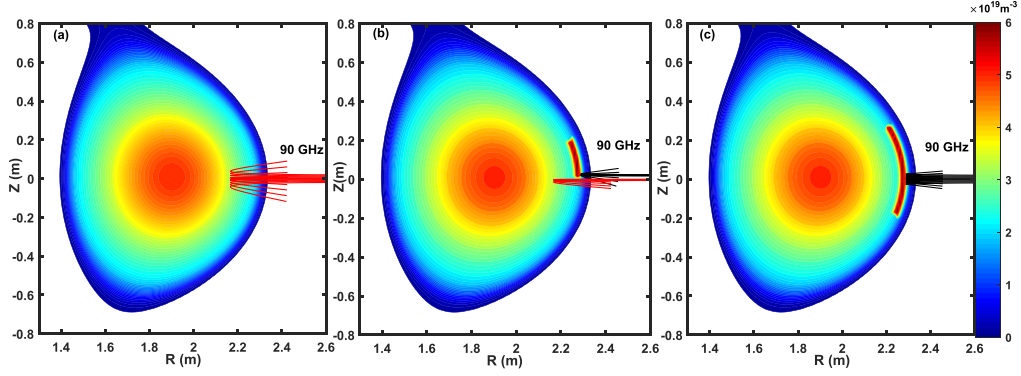


**Figure 4.** Ray-tracing simulation results of 90 GHz probing microwave in the W-band reflectometer during pellet homogenization.

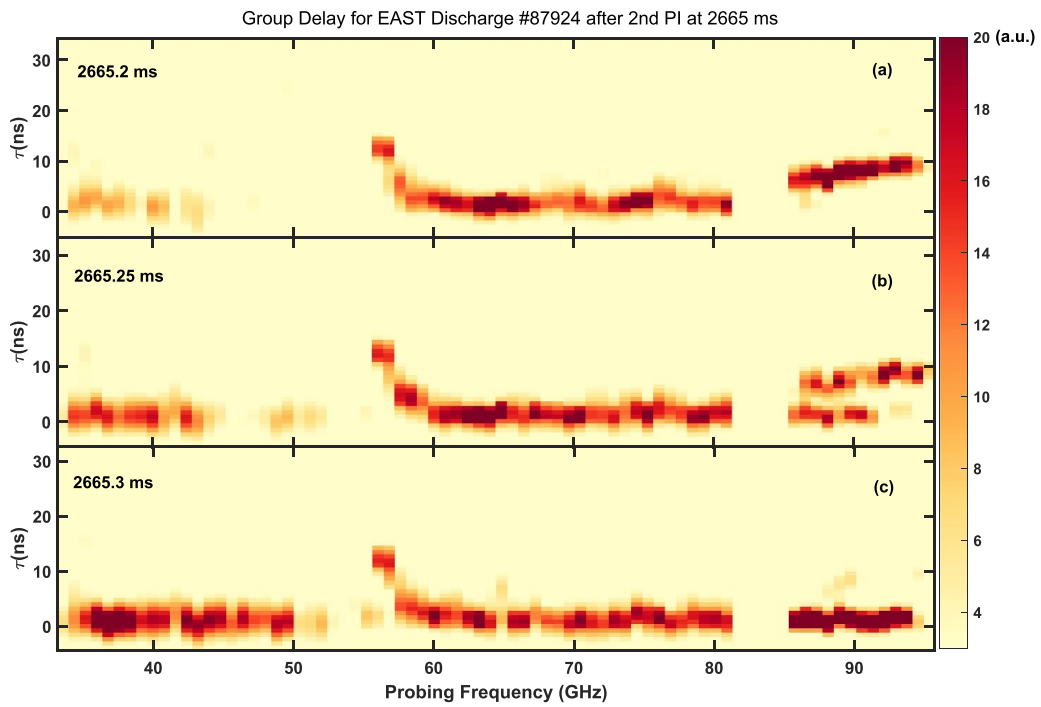


**Figure 5.** Group delay solely arising from microwave propagation in plasma after 2nd PI at 2665 ms. (a)  $T_{\text{period}} = 2665.2$  ms; (b)  $T_{\text{period}} = 2665.25$  ms; (c)  $T_{\text{period}} = 2665.3$  ms.

J-port, the ablated and ionized pellet particles are observed to deposit primarily in the edge region (as shown by figure 12). Simultaneously, the high-density pellet cloud undergoes a gradual poloidal expansion. When the ionized cloud's cross-section intersects with the reflectometer's detection path, the probing microwaves experience reflection. Given the several-centimeter beam width of the probing microwaves, as shown in figure 4(b), a fraction of these microwaves experiences cut-off reflection at the localized high-density region at the plasma edge, while another portion gets reflected by the cut-off layer in the plasma core. By analyzing changes in the group delay of microwaves as they propagating through the plasma, it becomes feasible to determine both the density and position of the localized high-density ablated clouds at that specific intersection. Consequently, the reflectometer can measure the

density increase localized at the edge, which is induced by the expansion process of pellet ablation.

The group delays arising solely from microwave propagation in the plasma at 2665.2 ms, 2665.25 ms, 2665.3 ms are further extracted and presented in figures 5(a)–(c), respectively. The group delay solely arising from microwave propagation in plasma ( $\tau$ ) can be determined by [21]:

$$\tau = \tau_{\text{wall}} - \tau_{\text{plasma}} + \frac{2(r_0 - r_{\text{wall}})}{2}. \quad (1)$$

The reflections labeled as  $\tau_{\text{wall}}$  and  $\tau_{\text{plasma}}$  correspond to the reflections from the inner vacuum wall and the plasma, respectively, both of which can be directly measured by the reflectometer.  $r_0$  denotes the position of the zero-density layer,

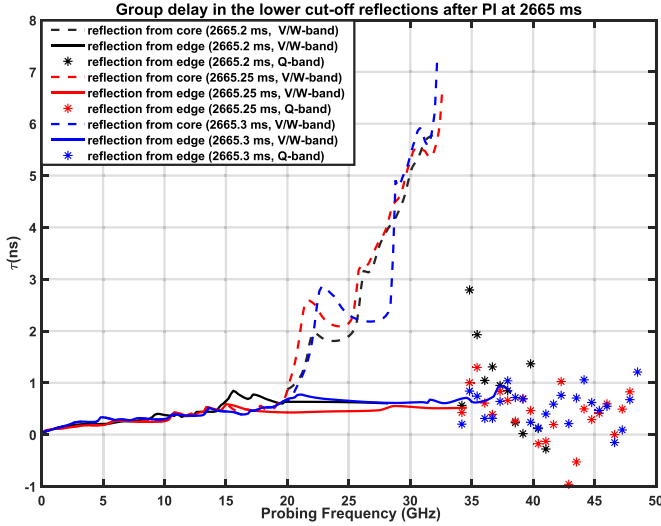


**Figure 6.** Comparison of group delay between the lower and upper cut-off reflections after 2nd PI at 2665 ms.

$r_{\text{wall}}$  represents the position of the inner wall and  $c$  corresponds to the velocity of probing microwave propagating in the vacuum.

In conjunction with the emergence of the lower cut-off reflection featuring a group delay of  $\sim 1$  ns in the Q-band, the upper cut-off reflection with a group delay of  $\sim 1$  ns is also observed. Further in the W-band reflectometer, which operates within a probing frequency range of 85 GHz–95 GHz, an intriguing ‘dual-reflection’ phenomenon becomes evident. This phenomenon manifests when probing microwaves of the same frequency encounter cut-off reflections at two distinct positions.

At 2665.2 ms, as shown in figure 5(a), the Q-band within the frequency range of 33 → 43 GHz demonstrates a lower cut-off reflection signal with a group delay approximately equal to 1 ns. In contrast, the W-band probing microwaves, functioning between 85 and 95 GHz, exhibit a stronger upper cut-off reflection signal with an extended group delay ranging from 4.8 ns to 9.5 ns. Furthermore, a faint upper cut-off reflection signal, possessing a group delay close to 1 ns, is also discernible near 86.5 GHz, mirroring the characteristics of the aforementioned lower cut-off reflection signal in the Q-band. Subsequent to intervals of 50  $\mu\text{s}$  and 100  $\mu\text{s}$ , as shown in figures 5(b) and (c), it becomes evident that a substantial intensification in low-group-delay signals transpires for both the upper cut-off reflections in the W-band and the lower cut-off reflections in the Q-band. Concurrently, there is a corresponding attenuation in high-group-delay signals for upper cut-off reflections in the W-band. During the occurrence of the ‘dual-reflection’ phenomenon observed in the reflectometer after PI, it is noteworthy that high-group-delay signals ( $\tau_{\text{plasma}} = 7 \sim 10$  ns), reflected from the core cut-off layer, coexist alongside low-group-delay signals ( $\tau_{\text{plasma}} \sim 1$  ns) reflected from the edge-localized high-density cut-off layer. On the other hand, in addition to the signal attenuation

linked to the heightened probing frequency, the total reflected power ( $P_{\text{total}}$ ) during the ‘dual-reflection’ phenomenon remains relatively unchanged. This experimental result corroborates the simulation results illustrated in figure 4(b).

Figure 6 shows the group delay measured by the lower cut-off reflections in Q-band reflectometer (dots represented by \*) and the equivalent group delay derived from the upper cut-off reflections at the edge (solid lines) and the core (dotted lines). The upper cut-off density profiles, initiated from a zero-density layer, are derived from the signals of upper cut-off reflections captured by the V- and W-band reflectometer. Using this density profile, the theoretical distribution of group delay for the lower cut-off reflections can be deduced. This calculated group delay for the lower cut-off reflection signal, expected to fall within the frequency range of 0–35 GHz, is subsequently juxtaposed with the experimental data obtained from the Q-band reflectometer (33–50 GHz). The method for contrasting the upper and lower cut-off reflections is outlined in detail in [26]. Remarkably, the lower cut-off reflection signal detected in the Q-band demonstrates a remarkable concordance with the upper cut-off reflection signal, distinguished by a low group delay. This alignment in behavior can be attributed to the formation of a high-density region after PI, predominantly localized at the edge. Consequently, both the lower cut-off probing microwaves in the Q-band and a fraction of the upper cut-off probing microwaves in the W-band encounter reflection within this edge-localized high-density region. Moreover, another portion of the W-band upper cut-off probing microwaves is reflected by the density cut-off layer in the core. However, as the ablated pellet particles proceed to vertically expand during 2665.2 ms → 2665.25 ms, resulting in the enlargement of this edge-localized high-density region, a portion of probing microwaves undergoes cut-off reflection due to interaction with the plasma at the edge. This phenomenon triggers the gradual attenuation and eventual disappearance of high-group-delay signals in the W-band. Simultaneously, there is a further enhancement in the low-group-delay signal present in both the Q-band lower cut-off reflections and the W-band upper cut-off reflections.

As shown in figure 3, the existence of low-group-delay signals in the upper cut-off reflections of the W-band and the enhancement of the lower cut-off reflections in the Q-band endure for approximately 1.7 ms. Subsequent to this phase, a gradual attenuation in the signal intensity of the Q-band lower cut-off reflection becomes evident, while the W-band upper cut-off signal gradually reverts to its pre-injection state, characterized by high-group-delay reflections. As the ablated pellet particles progressively assimilate into the background plasma, the edge-localized peak density subsides, consequently leading to a gradual return of the density profile to a monotonic distribution. Notably, throughout this diminishing process, the ‘dual-reflection’ phenomenon is also observed with opposing trends of evolution. This phenomenon suggests that both the edge-localized density peaks induced by PI and the minimum homogenization period of pellet plasmoid endure for approximately 1.7 ms, representing a temporal parameter for PI that

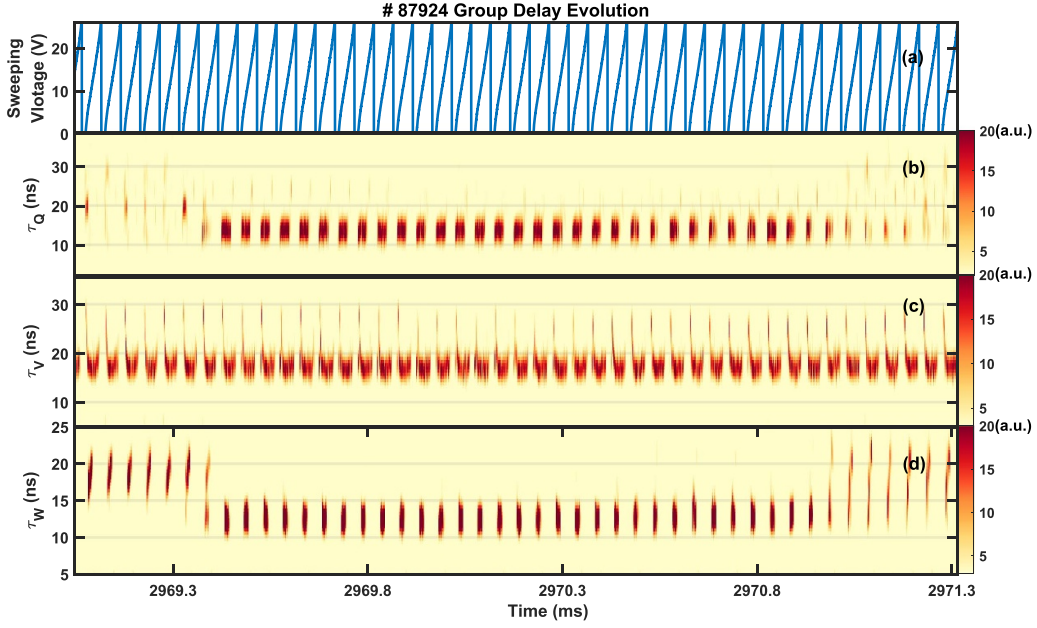


**Figure 7.** Evolution of group delay in density profile reflectometer after 5th PI at 2969 ms. (a) Input of VCO in reflectometer and group delay measured by (b) Q-band (33 → 50 GHz); (c) V-band (50 → 75 GHz); (d) W-band (75 → 110 GHz).

has been experimentally determined on EAST for the first time.

**3.1.2. Dual-reflection of Q-band lower cut-off probing microwave.** The progression of group delay in Q-, V- and W-band sub-systems after the 5th PI at 2.969 s is illustrated in figure 7. As the core plasma density further increased after the 5th PI, the high-group-delay lower cut-off reflections from the plasma core before 5th PI was successfully measured by the Q-band reflectometer. This is evident from the Q-band reflection signal (34 GHz → 45GHz) shown in figure 8(a). At 2969.35 ms and 2969.4 ms after the 5th PI at 2969 ms, the phenomenon of ‘dual reflection’ manifested in both the Q-band lower cut-off reflections and the W-band upper cut-off reflections, as shown in figures 8(a) and (b). A comparison between measurements obtained from two signals is presented in figures 9.

### 3.2. Local density increase measured by reflectometer and POINT

As shown in figure 10, the reflectometer has enabled, for the first time, the measurement of edge-localized peaking density profiles during the pellet homogenization process on EAST. This achievement is attributed to the introduction of the Q-band lower cut-off frequency (lower cut-off region indicated by the yellow dotted line) and the W-band upper cut-off frequency (upper cut-off region indicated by the cyan dotted line). This extension significantly augments the radial density coverage attainable by the reflectometer measurement. The existence of a blind region, positioned between the lower and upper cut-off regions, signifies that capturing reflections at the lower

cut-off in the core plasma presents greater challenges compared to those at the upper cut-off. The overlapped region between these cut-offs serves as a cross-validation mechanism for bench-marking purposes. Notably, the precise deposition positions of both the 2nd and 5th pellets have been determined to be localized within a radial span of approximately  $R = 2.28$  m, where  $\rho \sim 0.85$ . This measurement of the edge-localized peaking density profile provides the groundwork for a deeper analysis of how local density increases and ablated pellet particles undergo expansion.

As shown in figure 11, the evolution of line-integrated densities, as gauged by the 8th, 9th, and 10th chords of the POINT diagnostic system during PI discharge 87924 on EAST, is visually presented. The instants of density increase for each chord after PI are designated by blue diamonds with the criteria being that the normalized density increase exceeds 20%:

$$\delta \hat{n}_e = \frac{n_{e,\text{onset}} - \bar{n}_{e0}}{n_{e,\text{max}} - \bar{n}_{e0}} \geq 20\% \quad (2)$$

where  $n_{e,\text{onset}}$  denotes the time point ( $T_{\text{onset}}$ ) at which the density begins to exhibit increase after each PI,  $\bar{n}_{e0}$  represents the average density pre-injection, and  $n_{e,\text{max}}$  signifies the highest density reached post-injection. As shown in figures 11(a) and (b), the subsequent increase in line-integrated densities, successively observed in the 8th, 9th and 10th chords of POINT after 2nd PI at 2665 ms and 5th PI at 2969 ms, is in alignment with the local density surge registered by the reflectometer, thus corroborating the accuracy of both measurement techniques. Consequently, this validation sets the stage for the computation of the parallel expansion velocity.



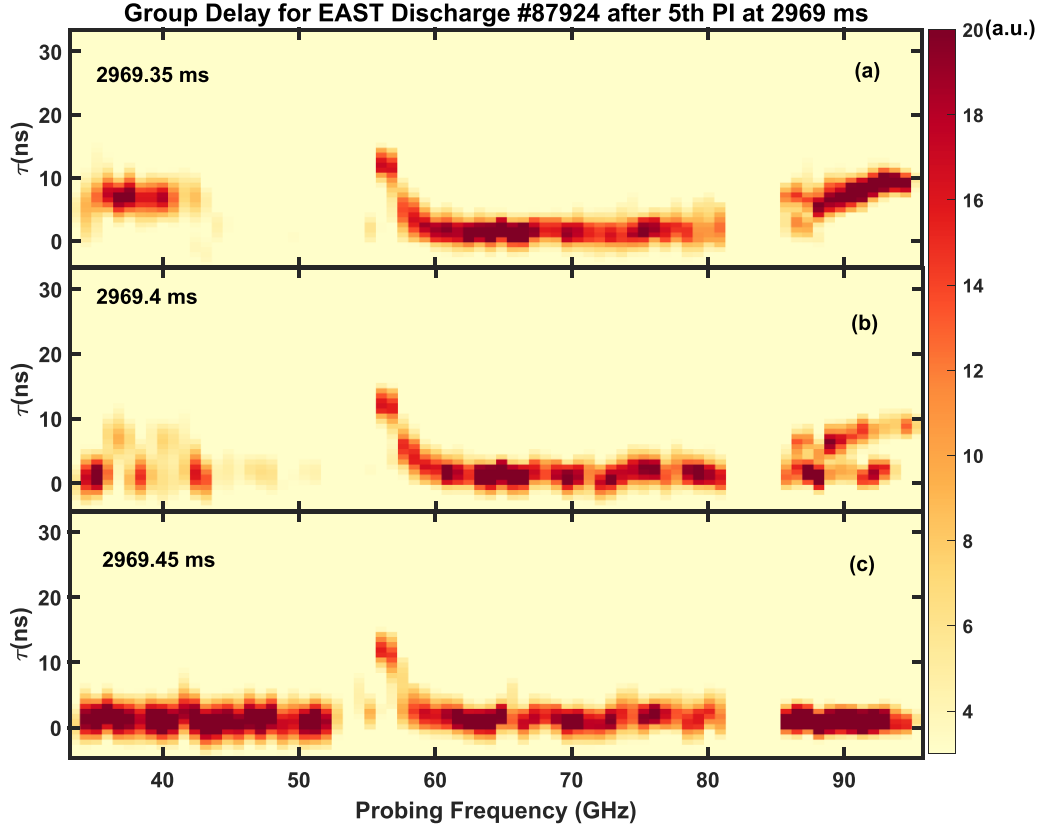


**Figure 8.** Group delay solely arising from microwave propagation in plasma after 5th PI at 2969 ms. (a)  $T_{\text{period}} = 2969.35$  ms; (b)  $T_{\text{period}} = 2969.4$  ms; (c)  $T_{\text{period}} = 2969.45$  ms.

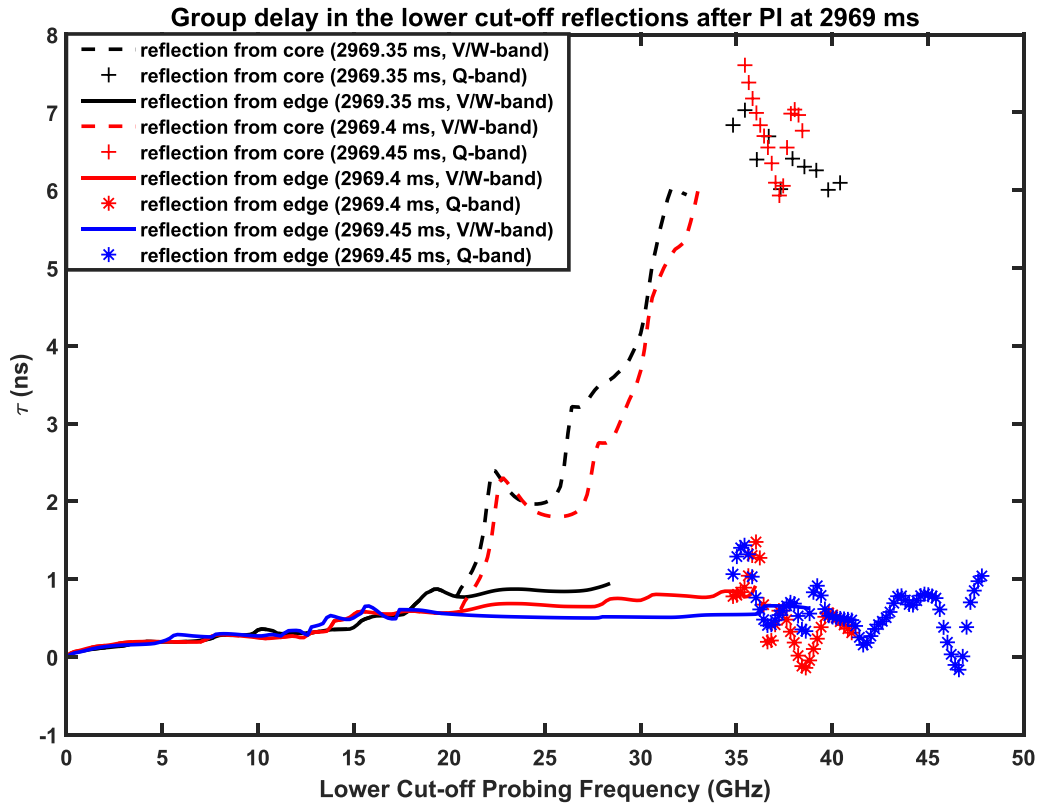


**Figure 9.** Comparison of group delay between the lower and upper cut-off reflections after 5th PI at 2969 ms.

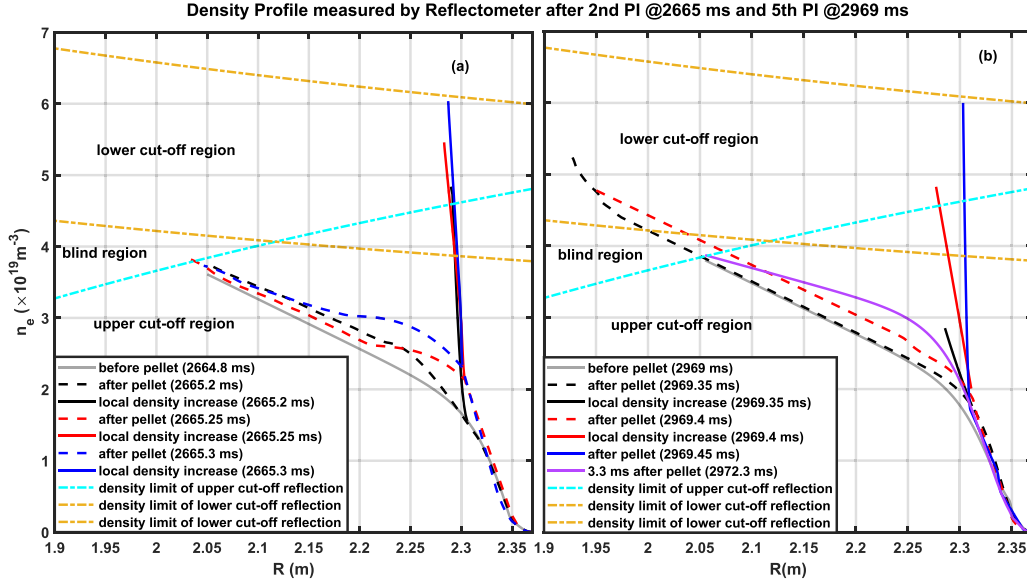


**Figure 10.** Density profiles measured by Reflectometer after the 2nd PI at 2665 ms and the 5th PI at 2969 ms on EAST. The lower cut-off region, blind region and the upper cut-off region are delineated by yellow and cyan dotted lines. The distinct localized peaking density profiles can be discerned and quantified through the observation of the ‘dual-reflection’ signals.

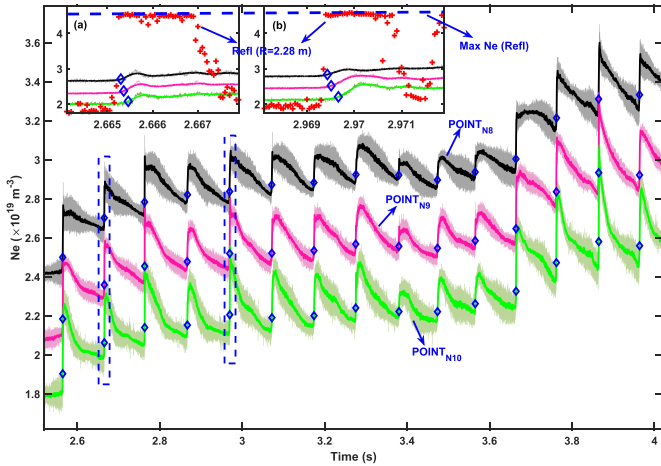


**Figure 11.** Evolution of local density at  $R = 2.28$  m measured by reflectometer and line-integrated densities measured by the 8th → 10th chords of POINT during EAST discharge 87924. The onsets of density increase of each chord after PI are indicated by blue diamonds. (a) The 2nd pellet at 2665 ms; (b) the 5th pellet at 2969 ms. Red crosses denote the local density at 2.28 m measured by reflectometer.

#### 4. Parallel and poloidal expansion during pellet homogenization

The investigation into the parallel expansion dynamics of pellet clouds after PI is extended through the combined utilization of the reflectometer and POINT diagnostics, as shown in figure 2. Let’s consider the example of the 5th PI at 2969 ms. In this case, the high-density cloud region extends along a magnetic flux tube segment, spanning a distance of  $L_{PI \rightarrow \text{Refl}} \sim 14.5$  m from its formation location along the parallel magnetic field lines to the diagnostic window of the reflectometer

(Refl), and extending towards the 8th-chord of POINT diagnostic ( $L_{PI \rightarrow \text{POINT}} \sim 18.2$  m). Consequently, the length of the magnetic flux tube that interconnects these two diagnostics is calculated as  $L_{\text{Refl} \rightarrow \text{POINT}} = L_{PI \rightarrow \text{POINT}} - L_{PI \rightarrow \text{Refl}} = 3.7$  m.

The precise determination of the onset time for the local density increase after the 5th PI is distinctly observed at  $T_{\text{onset}}(\text{Refl}) = 2969.325$  ms, as shown in figure 10, through the employment of the reflectometer measurements. Additionally, the onset time of  $T_{\text{onset}}(\text{POINT}) = 2969.43$  ms and the onset density of  $n_{e,\text{onset}}(\text{POINT}) = 2.841 \times 10^{19} \text{ m}^{-3}$  are deduced from the analysis of the measurement of 8th chord of POINT in figure 11(b). Consequently, the time difference between these two diagnostics can be computed as follows:

$$\Delta t = T_{\text{onset}}(\text{POINT}) - T_{\text{onset}}(\text{Refl}) = 105 \mu\text{s} \quad (3)$$

and the velocity of parallel expansion for high-density pellet clouds is

$$V_{\text{Paral}} = \frac{L_{\text{Refl} \rightarrow \text{POINT}}}{\Delta t} = 3.5238 \times 10^4 \text{ m s}^{-1}. \quad (4)$$

Furthermore, in addition to its propagation along the magnetic field lines towards the proximity of the reflectometer’s diagnostic window, the high-density plasmoid also undergoes an expansion in the poloidal plane. Here, we will call it poloidal expansion, which may encompass diffusion spreading, poloidal rotation, and the drift effect induced by  $\nabla B$ . Considering the notably faster rate of parallel expansion compared to poloidal expansion, the ablation cloud’s progression from the PI site to the neighboring region of the reflectometer measurement window is dominated by the parallel expansion process. As the expansion in the poloidal direction persists, the area of the ablation cloud with a high density gradually intersects with the probing region of the reflectometer. This gradual expansion covers the poloidal probing area ( $d \sim 4$  cm) of the

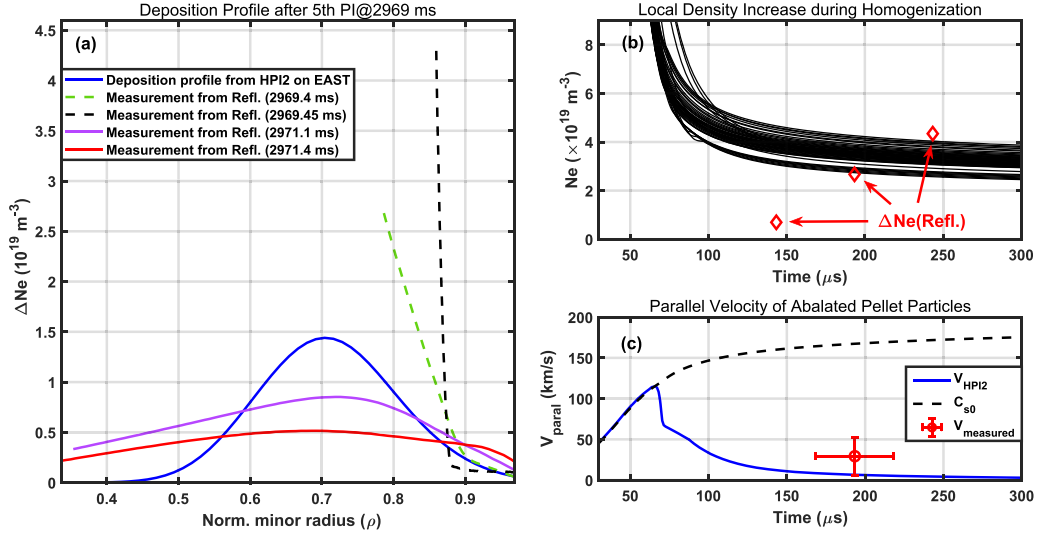


**Figure 12.** Comparison between experimental measurement and simulation results. (a) The deposition profiles obtained from HPI2 (blue line) and reflectometer measurement at 2971.1 ms (violet line) and 2971.4 ms after PI (red line). (b) Local density increase during homogenization. The average density of a sets of pellet ablation clouds at different positions simulated from HPI2 code (black curves) and the local density increase measured by reflectometer (red diamonds). (c) Parallel expansion velocity along magnetic field lines of ablated pellet particles. The local ion sound speed  $C_{s0}$  (black dotted line), the parallel expansion velocity obtained by HPI2 code (blue line) and measured by the combination of reflectometer and POINT diagnostics (red diamond).

reflectometer, where localized high-density regions at the edge flux surface, result in the temporary occurrence and vanishing of the ‘dual-reflection’ phenomenon. As depicted in figure 6, the duration for coverage is estimated to be  $T_{\text{cover}} = 125 \mu\text{s}$ . Consequently, the poloidal expansion velocity can be subsequently determined as:

$$V_{\text{pol}} = \frac{d}{T_{\text{cover}}} = 320 \text{ m s}^{-1}. \quad (5)$$

The statistical analysis of the poloidal expansion velocity of the high-density ablation cloud after each PI during discharges 87922 and 87924 on EAST, employing the outlined calculation methodology, yields an average velocity value of  $V_{\text{pol}} = (380.95 \pm 50.39) \text{ m s}^{-1}$ .

## 5. Discussion

For the analysis of pellet homogenization processes, a two-cell four-fluid model, as described in [1, 2, 27], was employed to simulate both the parallel expansion and the  $\nabla B$ -induced drift of the plasmoid. During the initial stages of homogenization [28], it is assumed that the parallel expansion speed of the plasmoid corresponds to the ion sound speed, after which viscosity becomes a significant factor. The expansion ceases upon achieving pressure equilibrium between the plasmoid and the surrounding background plasma. Regarding the  $\nabla B$ -induced drift, various damping mechanisms have been considered, including Alfvén wave propagation [7] and the influence of parallel resistive currents both outside (referred to as the Pégourié effects) [1] and inside the plasmoid (referred to as the Rozhansky effects [29]).

The experimental measurements of local density increase after PI plays a crucial role in enhancing and refining the HPI2 pellet simulation code on EAST [30, 31]. A comparison between experimental measurements and simulation results is presented in figure 12. In the course of the pellet deposition process, the deposited profiles after the 5th PI (2969 ms) during EAST discharge #87924 are further compared in figure 12(a). Both the simulation result and experimental measurements indicate that the deposition position is around  $\rho \sim 0.7$ . The observed variations in the deposition profile at 2969.45 ms (black dashed line), 2971.1 ms (violet solid line) and 2971.4 ms (red solid line) after PI suggest a progressive decline in peak density throughout the deposition process after PI.

During the homogenization process, a series of high-density clouds emerge along the trajectory of injection. As shown in figure 12(b), with increasing homogenization time, the extent of high-density clouds along the magnetic flux tube elongates while the mean density gradually diminishes. Furthermore, as shown in figure 2, the parallel expansion of the high-density clouds encompasses a magnetic flux tube segment with a length  $L \sim 14.5 \text{ m}$ , starting from its origin along the magnetic field lines and extending to reach the reflectometer’s diagnostic window. Assuming an expansion velocity equivalent to the local ion sound speed  $C_{s0}$ , the expansion time is estimated to be about  $143.4 \mu\text{s}$ . Throughout the parallel and poloidal expansion of the pellet ablation cloud, the reflectometer enables the evaluation of temporal density variations at a designated position. Specifically, as the ablation cloud reaches the area of detection for the reflectometer, the temporal variations in the localized density enhancement caused by the ablation cloud can be calculated, as illustrated by the

solid black, red, and blue lines in figure 10(b). This localized density in the plasmoid, identified by the reflectometer during the homogenization process, is denoted by the red diamonds in figure 12(b).

The parallel expansion velocity ( $V_{\text{HPI2}}$ ) accounting for viscous effects in the HPI2 pellet simulation is depicted by the solid blue line in figure 12(c), whereas  $C_{s0}$  is denoted by the dashed black line. Furthermore, through the synergy of the reflectometer and POINT diagnostic systems, the parallel expansion velocity of the pellet ablation cloud can be measured experimentally. In the discharges 87922 and 87924 on EAST, employing the aforementioned calculation approach, statistical analysis of the parallel expansion velocity of the high-density ablation cloud after each PI was performed. The computed outcomes are presented below:  $V_{\text{measured}} = (2.93 \pm 2.34) \times 10^4 \text{ m s}^{-1}$  (red diamonds in figure 12(c)). Remarkably, this measured value is in alignment with the findings reported from the TFTR experiment [13]. Importantly, it should be underscored that the experimentally determined velocity closely approximates  $V_{\text{HPI2}}$  and is notably lower than  $C_{s0}$ . This observation accentuates the infeasibility of directly adopting  $C_{s0}$  as the parallel expansion velocity for the pellet ablation cloud in simulations employing the HPI2 code for EAST PI experiments. To address this, a more comprehensive examination of various parameters affecting this process is necessary, including the incorporation of viscous effects. On the other hand, when dealing with the subsequent poloidal expansion after the plasmoid reaches the neighboring region of the reflectometer measurement window, it incorporates only the diffusion effect in the current HPI2 simulation for the EAST case, leading to a simulated poloidal diffusion velocity (approximately several ten  $\text{m s}^{-1}$ ) that notably deviates from the values obtained through experimental measurements (approximately  $380.95 \text{ m s}^{-1}$ ). The investigation into the comparison of the poloidal expansion velocity between the experimental measurement and HPI2 simulation will be pursued in subsequent research endeavors. This comprehensive consideration will be pivotal in the successful application of the HPI2 pellet simulation code on EAST.

## 6. Summary

The conventional X-mode polarized microwave reflectometer, operating based on the upper cut-off frequency, is inherently constrained to offering only monotonic density profiles, lacking the capacity to effectively measure density profiles featuring both high-density and edge-localized peaking characteristics after PI. This research introduces an innovative methodology for assessing the local density increase after PI, utilizing the distinctive ‘dual-reflection’ phenomena observed in the EAST microwave reflectometer, which harnesses measurements from both the X-mode lower and upper cut-off frequencies. The implementation of this pioneering technique on EAST signifies a significant advancement, enabling a comprehensive exploration of density profiles ranging from the edge to the core region. Importantly, this approach accommodates density profiles characterized by edge-localized peaks, thus

substantially enhancing our analytical capabilities in high-density experiments after PI.

Subsequent to this, an extensive experimental investigation was undertaken on EAST to comprehensively explore the parallel and poloidal expansion dynamics of the pellet ablation cloud. The determined velocity for parallel expansion was approximately  $(2.93 \pm 2.34) \times 10^4 \text{ m s}^{-1}$ , while the velocity associated with poloidal expansion was measured at approximately  $(380.95 \pm 50.39) \text{ m s}^{-1}$ . Initially, a comparative assessment was made between these experimental measurements and simulation outcomes derived from the HPI2 code. The alignment of the deposition profiles between experimental observations and simulation results notably indicated a significant degree of consistency in terms of deposition position. Furthermore, the velocity measurements for both the parallel and poloidal expansion of pellet plasmoid, as conducted in this study, serve to enrich our comprehensive understanding of the homogenization process that transpires after PI. This advancement represents a pivotal stride towards facilitating the application of the HPI2 code in EAST PI experiments.

In the PI experiments during L-mode on EAST, the phenomenon of ‘dual reflections’ observed in the reflectometer enabled the successful measurement of edge-localized high-density profiles during the pellet ablation. However, to enhance the generality of this approach, further steps are required in upcoming work. It involves extending the applicability of this method by conducting PI experiments under conditions such as the H-mode plasma, allowing for thorough parameter scans of the plasma, thereby validating the method’s universality. Furthermore, the present frequency-sweeping period of the reflectometer system on the EAST is  $50 \mu\text{s}$ , close to the time duration of the homogenization process in present case ( $100\text{--}150 \mu\text{s}$ ), rendering it challenging to effectively analyze the rapid parallel and poloidal expansion process of the ablative cloud at this level of time resolution. Therefore, our subsequent endeavor involves to reduce the frequency-sweeping period to less than  $10 \mu\text{s}$ , with the aim of further investigating the deposition process of the ablation cloud.

## Acknowledgments

This work was supported by the National Key R&D Program of China (Grant Nos. 2022YFE03050003, 2019YFE03040002, 2019YFE03080200, 2022YFE03020004, 2022YFE03070004 and 2017YFE0301205), the National Natural Science Foundations of China (Grant Nos. 11975271, 12275315, 12075284, 12175277 and 11875289) and China Postdoctoral Science Foundation (Grant No. 2021M703256) and the China National Postdoctoral Program for Innovative Talents (BX20230371 to Chenguang Wan).

## ORCID iDs

J. Huang  <https://orcid.org/0000-0001-6289-1812>  
 T. Zhang  <https://orcid.org/0000-0002-1555-6226>  
 Y.F. Liang  <https://orcid.org/0000-0002-9483-6911>  
 J.L. Hou  <https://orcid.org/0000-0002-7109-5700>

K.X. Ye  <https://orcid.org/0000-0003-0927-4502>  
 K.N. Geng  <https://orcid.org/0000-0001-7808-0192>  
 H.M. Xiang  <https://orcid.org/0000-0001-7799-6190>  
 H.Q. Liu  <https://orcid.org/0000-0001-6892-358X>  
 A. Krämer-Flecken  <https://orcid.org/0000-0003-4146-5085>  
 X. Gao  <https://orcid.org/0000-0003-1885-2538>

## References

- [1] Pégourié B. 2007 *Plasma Phys. Control. Fusion* **49** R87
- [2] Pégourié B. et al 2004 *Plasma Phys. Control. Fusion* **47** 17
- [3] Yan L.W., Xiao Z.G., Zheng Y.J., Dong J., Deng Z., Li B., Li L.i., Feng Z., Liu Y. and Wang E. 2002 *Nucl. Fusion* **42** 265
- [4] Parks P.B. and Turnbull R.J. 1978 *Phys. Fluids* **21** 1735–41
- [5] Pégourié B. and Picchiottino J.-M. 1996 *Phys. Plasmas* **3** 4594–605
- [6] de Kloe J., Noordermeer E., Cardozo N.J.L. and Oomens A.A.M. 1999 *Phys. Rev. Lett.* **82** 2685–8
- [7] Parks P.B., Sessions W.D. and Baylor L.R. 2000 *Phys. Plasmas* **7** 1968–75
- [8] Baylor L.R. et al 1992 *Nucl. Fusion* **32** 2177
- [9] Matsuyama A., Sakamoto R., Yasuhara R., Funaba H., Uehara H., Yamada I., Kawate T. and Goto M. 2022 *Phys. Rev. Lett.* **129** 255001
- [10] Panadero N. et al 2023 *Nucl. Fusion* **63** 046022
- [11] Futatani S., Huijsmans G., Loarte A., Baylor L.R., Commaux N., Jernigan T.C., Fenstermacher M.E., Lasnier C., Osborne T.H. and Pegourié B. 2014 *Nucl. Fusion* **54** 073008
- [12] Futatani S., Pamela S., Garzotti L., Huijsmans G.T.A., Hoelzl M., Frigione D. and Lennholm M. 2019 *Nucl. Fusion* **60** 026003
- [13] Mansfield D.K., Janos A., Owens D.K., Schmidt G.L., Bell M.G., Cavallo A., Fredrickson E., Ramsey A.T. and Taylor G. 1991 *Phys. Rev. Lett.* **66** 3140–3
- [14] Funaba H., Yasuhara R., Uehara H., Yamada I., Sakamoto R., Osakabe M. and Den Hartog D.J. 2022 *Sci. Rep.* **12** 15112
- [15] Hou J.L. et al 2019 *Fusion Eng. Des.* **145** 79–86
- [16] Yao X.J. et al 2017 *Nucl. Fusion* **57** 066002
- [17] Huang J. et al 2020 *Nucl. Fusion* **60** 082008
- [18] Zou Z.Y. et al 2014 *Rev. Sci. Instrum.* **85** 11D409
- [19] Qu H. et al 2015 *Plasma Sci. Technol.* **17** 985
- [20] Zhang S.B., Gao X., Ling B.L., Wang Y., Zhang T., Han X., Liu Z., Bu J. and Li J. 2014 *Plasma Sci. Technol.* **16** 311
- [21] Wang Y.M., Gao X., Ling B.L., Zhang S.B., Zhang T., Han X., Liu S.C., Liu Z.X., Liu Y. and Ti A. 2013 *Fusion Eng. Des.* **88** 2950–5
- [22] Li C.Z., Hu J.S., Chen Y., Vinyar I.V., Li J.G. and Lukin Y. 2014 *Fusion Eng. Des.* **89** 99–103
- [23] Hou J.L. et al 2022 *Plasma Phys. Control. Fusion* **64** 055010
- [24] Mazzucato E. 1998 *Rev. Sci. Instrum.* **69** 2201–17
- [25] Conway G.D. 2006 *Nucl. Fusion* **46** S665
- [26] Huang J. et al 2022 *Plasma Sci. Technol.* **24** 055104
- [27] Pégourié B., Köchl F., Nehme H. and Polevoi A.R. 2009 *Plasma Phys. Control. Fusion* **51** 124023
- [28] Köchl F. et al 2012 Modelling of pellet particle ablation and deposition: the hydrogen pellet injection code HPI2 *EUROfusion Preprint EFDA-JET-PR* (posted online 3 December 2012, accessed 20 November 2014) (available at: <https://scipub.euro-fusion.org/wp-content/uploads/2014/11/EFDP12061.pdf>)
- [29] Rozhansky V., Senichenkov I., Veselova I. and Schneider R. 2004 *Plasma Phys. Control. Fusion* **46** 575
- [30] Zhang J. and Parks P. 2020 *Nucl. Fusion* **60** 066027
- [31] Zhang J., McClenaghan J., Parks P., Lao L. and Wu W. 2022 *Nucl. Fusion* **62** 086012